

DOUBLE-DETONATION SUB-CHANDRASEKHAR SUPERNOVAE: SYNTHETIC OBSERVABLES FOR MINIMUM HELIUM SHELL MASS MODELS

M. KROMER, S. A. SIM, M. FINK, F. K. RÖPKE, I. R. SEITENZAHL AND W. HILLEBRANDT
Max-Planck-Institut für Astrophysik, Karl-Schwarzschild-Straße 1, D-85748 Garching b. München, Germany
Draft version October 22, 2018

ABSTRACT

In the double detonation scenario for Type Ia supernovae it is suggested that a detonation initiates in a shell of helium-rich material accreted from a companion star by a sub-Chandrasekhar-mass White Dwarf. This shell detonation drives a shock front into the carbon-oxygen White Dwarf that triggers a secondary detonation in the core. The core detonation results in a complete disruption of the White Dwarf. Earlier studies concluded that this scenario has difficulties in accounting for the observed properties of Type Ia supernovae since the explosion ejecta are surrounded by the products of explosive helium burning in the shell. Recently, however, it was proposed that detonations might be possible for much less massive helium shells than previously assumed (Bildsten et al. 2007). Moreover, it was shown that even detonations of these minimum helium shell masses robustly trigger detonations of the carbon-oxygen core (Fink et al. 2010). Therefore it is possible that the impact of the helium layer on observables is less than previously thought. Here, we present time-dependent multi-wavelength radiative transfer calculations for models with minimum helium shell mass and derive synthetic observables for both the optical and γ -ray spectral regions. These differ strongly from those found in earlier simulations of sub-Chandrasekhar-mass explosions in which more massive helium shells were considered. Our models predict light curves which cover both the range of brightnesses and the rise and decline times of observed Type Ia supernovae. However, their colours and spectra do not match the observations. In particular, their $B - V$ colours are generally too red. We show that this discrepancy is mainly due to the composition of the burning products of the helium shell of the Fink et al. (2010) models which contain significant amounts of titanium and chromium. Using a toy model, we also show that the burning products of the helium shell depend crucially on its initial composition. This leads us to conclude that good agreement between sub-Chandrasekhar-mass explosions and observed Type Ia supernovae may still be feasible but further study of the shell properties is required.

Subject headings: methods: numerical – radiative transfer – supernovae: general

1. INTRODUCTION

Although the standard single-degenerate (SD) Chandrasekhar-mass scenario (see Hillebrandt & Niemeyer 2000 for a review) is capable of explaining most of the observed diversity of Type Ia supernovae (SNe Ia) (Höflich & Khokhlov 1996; Kasen et al. 2009) via the delayed-detonation (Khokhlov 1991) model, it suffers from severe problems in explaining the observed rate of SNe Ia. In particular, binary evolution population synthesis calculations predict rates which are an order of magnitude too low compared to the observed rate of SNe Ia (Ruiter et al. 2009, but see Meng & Yang 2010). In addition, recent observational studies suggest that Chandrasekhar-mass explosions of hydrogen-accreting carbon-oxygen (C/O) White Dwarfs (WDs) in SD binary systems cannot account for all SNe Ia: Gilfanov & Bogdán (2010) found that the X-ray flux of nearby elliptical galaxies is significantly weaker than expected for a population of WDs accreting hydrogen towards the Chandrasekhar-mass needed to explain the observed supernova rate in elliptical galaxies (see also Di Stefano 2010). Moreover, there is growing observational evidence that there are different populations of SNe Ia (Mannucci et al. 2005; Scannapieco & Bildsten 2005).

This has led to a revived interest in alternative explo-

sion mechanisms. Here we consider the double detonation scenario applied to sub-Chandrasekhar-mass C/O WDs. In that scenario a helium-accreting C/O WD explodes below M_{Ch} due to a detonation in the accreted helium shell which triggers a secondary core detonation by compressional heating (Woosley & Weaver 1994; Livne & Arnett 1995; Fink et al. 2007). This model has some very appealing features. Depending on the initial mass of the WD, a wide range of explosion strengths can be realized (e.g. Woosley & Weaver 1994; Livne & Arnett 1995; Höflich & Khokhlov 1996). Moreover, population synthesis studies (Ruiter et al. 2009) predict rates comparable to the observed galactic supernova rate.

However, earlier work (Höflich & Khokhlov 1996; Höflich et al. 1996; Nugent et al. 1997) found light curves and spectra of such models to be in conflict with the observed spectra and light curves of SNe Ia. The differences were mainly attributed to the composition of the outer layers. Due to the initial helium detonation in the outer shell, the ejecta of sub-Chandrasekhar-mass models are surrounded by a layer of helium and its burning products (which can include iron-peak nuclei). This, however, is in apparent contradiction to the layered composition structure of observed SNe Ia, where the composition changes from iron-group elements in the core to lower mass elements in the outer layers.

In a preceding paper Sim et al. (2010) have shown

that artificial explosions of “naked” sub-Chandrasekhar-mass WDs can reproduce the observed diversity of SNe Ia. Thus it is natural to ask if somewhat modified properties in the initial helium shells of realistic sub-Chandrasekhar-mass models can reduce the negative post-explosion effect of this shell on the observables. In particular, Bildsten et al. (2007) recently presented new calculations, indicating that detonations might occur for much less massive helium shells than previously thought. Fink et al. (2010) adopted the minimum helium shell masses of Bildsten et al. (2007) and investigated whether such low-mass helium detonations are capable of triggering a secondary detonation in the C/O core of the WD. In that study, they concluded that as soon as a detonation in the helium shell initiates, a subsequent core detonation is virtually inevitable. For example, they found that even a helium shell mass as low as $0.039 M_{\odot}$ is sufficient to detonate a C/O WD of $1.125 M_{\odot}$.

Here, we focus on the observable properties of the models presented in Fink et al. (2010) and their comparison to real SNe Ia. In particular, we investigate whether the low helium shell masses of these models help to alleviate the problems encountered previously when comparing double detonation sub-Chandrasekhar-mass models to observed spectra and light curves of SNe Ia (Höflich & Khokhlov 1996; Nugent et al. 1997).

The outline of the paper is as follows: in Section 2 we give a short summary of the models of Fink et al. (2010) before briefly describing details of our radiative transfer simulations in Section 3. In Section 4 we present synthetic observables for the Fink et al. (2010) models and compare them to the observed properties of SNe Ia. The results of this comparison and implications for future work on sub-Chandrasekhar-mass double detonations are discussed in Section 5. Finally, we draw conclusions in Section 6.

2. MODELS

Adopting the minimum helium shell masses required to initiate a helium detonation in the shell according to Bildsten et al. (2007), Fink et al. (2010) investigated the double detonation scenario for six models representing a range of different C/O core masses (the model parameters are summarized in Table 1). In all their models, they ignite an initial helium detonation in a single point at the base of the helium shell located on the positive z -axis (hereafter referred to as the “north-pole” of the WD). From there the helium detonation wave sweeps around the WD core until it converges at the south pole. At the same time a shock wave propagates into the core and converges at a point off-centre. Finding conditions that might be sufficient to initiate a core detonation in a finite volume around this point, Fink et al. (2010) then trigger a secondary core detonation at that point. This secondary detonation disrupts the entire WD and yields ejecta with a characteristic abundance distribution which is shown for Model 3 of Fink et al. (2010) in Figure 1.

In the initial helium shell the burning does not reach nuclear statistical equilibrium due to the low densities. Thus it mainly produces iron-group elements lighter than ^{56}Ni such as titanium, chromium and iron – including some amount of the radioactive isotopes ^{48}Cr and ^{52}Fe . Aside from a small mass of calcium, no significant

amounts of intermediate-mass elements are produced in the shell. However, a large fraction of helium remains unburned.

The core detonation yields both iron-group and intermediate-mass elements, the relative amounts of which depend crucially on the core density and thus WD mass. Models with more massive WDs produce more iron-group material and less intermediate-mass elements (similar to the explosions of the naked sub-Chandrasekhar-mass WDs studied in Sim et al. 2010). The most massive Model 6 of the sequence of Fink et al. (2010) produces almost only iron-group material and hardly any intermediate-mass elements (the most important burning products in the shell and core of the different models are listed in Table 1).

Due to the single-point ignition the models show strong ejecta asymmetries which can be divided into two main categories. First, the helium shell contains more iron-group material on the northern hemisphere as discussed by Fink et al. (2010). Second, the ignition point of the secondary core detonation is offset from the centre-of-mass of the model due to the off-centre convergence of the shock waves from the helium detonation.

3. RADIATIVE TRANSFER SIMULATIONS

To derive synthetic observables for the models, we performed radiative transfer simulations with the time-dependent multi-dimensional Monte Carlo radiative transfer code ARTIS described by Kromer & Sim (2009) and Sim (2007). Since the models produce significant amounts of ^{48}Cr and ^{52}Fe , we extended ARTIS to take into account the energy released by the decay sequences $^{52}\text{Fe} \rightarrow ^{52}\text{Mn} \rightarrow ^{52}\text{Cr}$ and $^{48}\text{Cr} \rightarrow ^{48}\text{V} \rightarrow ^{48}\text{Ti}$ in addition to the radioactive decays of $^{56}\text{Ni} \rightarrow ^{56}\text{Co}$ and $^{56}\text{Co} \rightarrow ^{56}\text{Fe}$ which form the primary energy source of SNe Ia (Truran et al. 1967, Colgate & McKee 1969). For other radioactive nuclei which are synthesized during the explosion in a non-negligible amount (e.g. ^{44}Ti in the shell) the life times are much longer than those of the ^{56}Ni decay-sequence. Thus they can be neglected at early times when the decays of ^{56}Ni and ^{56}Co power the light curves.

The total γ -ray energy E_{tot} that will be emitted from $t = 0$ to $t \rightarrow \infty$ in the decay chains we consider, will be

$$E_{\text{tot}} = (E_{^{56}\text{Ni}} + E_{^{56}\text{Co}}) \frac{M_{^{56}\text{Ni}}}{m_{^{56}\text{Ni}}} + (E_{^{52}\text{Fe}} + E_{^{52}\text{Mn}}) \frac{M_{^{52}\text{Fe}}}{m_{^{52}\text{Fe}}} + (E_{^{48}\text{Cr}} + E_{^{48}\text{V}}) \frac{M_{^{48}\text{Cr}}}{m_{^{48}\text{Cr}}}. \quad (1)$$

Here $E_{^{56}\text{Ni}}$, $(E_{^{56}\text{Co}}, E_{^{52}\text{Fe}}, E_{^{52}\text{Mn}}, E_{^{48}\text{Cr}}, E_{^{48}\text{V}})$ is the mean energy emitted per decay of ^{56}Ni , (^{56}Co , ^{52}Fe , ^{52}Mn , ^{48}Cr , ^{48}V). Similarly, $M_{^{56}\text{Ni}}$ ($M_{^{52}\text{Fe}}, M_{^{48}\text{Cr}}$) is the initial mass of ^{56}Ni (^{52}Fe , ^{48}Cr) synthesized in the explosion and $m_{^{56}\text{Ni}}$ ($m_{^{52}\text{Fe}}, m_{^{48}\text{Cr}}$) the mass of the ^{56}Ni (^{52}Fe , ^{48}Cr) atom.

Following Lucy (2005), this energy is quantized into $\mathcal{N} = E_{\text{tot}}/\epsilon_0$ identical indivisible energy “pellets” of initial co-moving frame (cmf) energy ϵ_0 . The pellets are first assigned to one of the decay sequences in proportion to the amount of energy deposited in the different decay sequences (terms on the right-hand-side of Equation 1). Then they are distributed on the grid accord-

Table 1
Parameters of our model sequence.

Model	1	2	3	4	5	6	3c	3m
M_{tot}	0.936	1.004	1.080	1.164	1.293	1.3885	1.025	1.071
M_{core}	0.810	0.920	1.025	1.125	1.280	1.3850	1.025	1.025
$M_{\text{core}}(^{56}\text{Ni})^{\text{a}}$	1.7×10^{-1}	3.4×10^{-1}	5.5×10^{-1}	7.8×10^{-1}	1.05	1.10	5.5×10^{-1}	5.6×10^{-1}
$M_{\text{core}}(^{52}\text{Fe})^{\text{a}}$	7.6×10^{-3}	9.9×10^{-3}	9.6×10^{-3}	7.9×10^{-3}	4.2×10^{-3}	1.7×10^{-4}	9.6×10^{-3}	9.4×10^{-3}
$M_{\text{core}}(^{48}\text{Cr})^{\text{a}}$	3.9×10^{-4}	4.6×10^{-4}	4.5×10^{-4}	3.8×10^{-4}	2.1×10^{-4}	7.1×10^{-5}	4.5×10^{-4}	4.4×10^{-4}
$M_{\text{core}}(^{44}\text{Ti})$	7.2×10^{-6}	9.0×10^{-6}	1.1×10^{-5}	1.4×10^{-5}	1.4×10^{-5}	9.9×10^{-6}	1.1×10^{-5}	1.2×10^{-5}
$M_{\text{core}}(^{40}\text{Ca})$	2.0×10^{-2}	2.1×10^{-2}	1.8×10^{-2}	1.4×10^{-2}	6.9×10^{-3}	1.8×10^{-3}	1.8×10^{-2}	1.8×10^{-2}
$M_{\text{core}}(^{36}\text{Ar})$	2.2×10^{-2}	2.2×10^{-2}	1.9×10^{-2}	1.5×10^{-2}	6.7×10^{-3}	1.7×10^{-3}	1.9×10^{-2}	1.9×10^{-2}
$M_{\text{core}}(^{32}\text{S})$	1.3×10^{-1}	1.2×10^{-1}	1.0×10^{-1}	7.5×10^{-2}	3.3×10^{-2}	8.0×10^{-3}	1.0×10^{-1}	1.0×10^{-1}
$M_{\text{core}}(^{28}\text{Si})$	2.7×10^{-1}	2.5×10^{-1}	2.1×10^{-1}	1.4×10^{-1}	6.1×10^{-2}	1.5×10^{-2}	2.1×10^{-1}	2.0×10^{-1}
$M_{\text{core}}(^{24}\text{Mg})$	4.5×10^{-2}	3.5×10^{-2}	2.4×10^{-2}	1.1×10^{-2}	9.3×10^{-3}	4.3×10^{-3}	2.4×10^{-2}	2.2×10^{-2}
$M_{\text{core}}(^{16}\text{O})$	1.4×10^{-1}	1.1×10^{-1}	8.0×10^{-2}	4.2×10^{-2}	3.1×10^{-2}	1.2×10^{-2}	8.0×10^{-2}	7.7×10^{-2}
$M_{\text{core}}(^{12}\text{C})$	6.6×10^{-3}	4.4×10^{-3}	2.7×10^{-3}	8.8×10^{-4}	5.9×10^{-3}	7.4×10^{-4}	2.7×10^{-3}	3.3×10^{-3}
M_{sh}	0.126	0.084	0.055	0.039	0.013	0.0035	–	0.046
$M_{\text{sh}}(^{56}\text{Ni})^{\text{a}}$	8.4×10^{-4}	1.1×10^{-3}	1.7×10^{-3}	4.4×10^{-3}	1.5×10^{-3}	5.7×10^{-4}	–	1.1×10^{-8}
$M_{\text{sh}}(^{52}\text{Fe})^{\text{a}}$	7.6×10^{-3}	7.0×10^{-3}	6.2×10^{-3}	3.5×10^{-3}	1.2×10^{-3}	2.0×10^{-4}	–	6.1×10^{-9}
$M_{\text{sh}}(^{48}\text{Cr})^{\text{a}}$	1.1×10^{-2}	7.8×10^{-3}	4.4×10^{-3}	2.2×10^{-3}	6.8×10^{-4}	1.5×10^{-4}	–	7.9×10^{-8}
$M_{\text{sh}}(^{44}\text{Ti})$	7.9×10^{-3}	5.4×10^{-3}	3.4×10^{-3}	1.8×10^{-3}	4.9×10^{-4}	6.2×10^{-5}	–	4.2×10^{-5}
$M_{\text{sh}}(^{40}\text{Ca})$	4.7×10^{-3}	3.2×10^{-3}	2.2×10^{-3}	2.2×10^{-3}	6.8×10^{-4}	2.4×10^{-4}	–	3.5×10^{-3}
$M_{\text{sh}}(^{36}\text{Ar})$	5.0×10^{-3}	3.2×10^{-3}	2.0×10^{-3}	1.6×10^{-3}	5.2×10^{-4}	1.3×10^{-4}	–	2.7×10^{-2}
$M_{\text{sh}}(^{32}\text{S})$	2.2×10^{-3}	1.2×10^{-3}	7.8×10^{-4}	1.3×10^{-3}	4.3×10^{-4}	1.9×10^{-4}	–	1.4×10^{-2}
$M_{\text{sh}}(^{28}\text{Si})$	4.8×10^{-4}	2.5×10^{-4}	1.4×10^{-4}	4.7×10^{-4}	1.6×10^{-4}	1.3×10^{-4}	–	5.9×10^{-4}
$M_{\text{sh}}(^{24}\text{Mg})$	4.3×10^{-5}	2.3×10^{-5}	1.3×10^{-5}	1.0×10^{-4}	3.8×10^{-5}	3.6×10^{-5}	–	3.0×10^{-5}
$M_{\text{sh}}(^{16}\text{O})$	3.2×10^{-6}	1.7×10^{-6}	1.9×10^{-6}	6.0×10^{-5}	2.1×10^{-5}	2.6×10^{-5}	–	1.0×10^{-5}
$M_{\text{sh}}(^{12}\text{C})$	1.2×10^{-3}	5.3×10^{-4}	2.2×10^{-4}	7.9×10^{-5}	1.7×10^{-5}	1.6×10^{-6}	–	3.2×10^{-5}
$M_{\text{sh}}(^4\text{He})$	8.3×10^{-2}	5.3×10^{-2}	3.3×10^{-2}	2.0×10^{-2}	6.9×10^{-3}	1.7×10^{-3}	–	2.7×10^{-4}
$\Delta m_{15}(B)$ / mag	0.88	1.25	1.74	1.77	1.23	1.29	1.63	1.37
$t_{\text{max}}(B)$ / days	17.0	17.0	17.7	16.4	15.2	14.3	18.2	18.1
$M_{\text{B,max}}$ / mag	-15.9	-17.3	-18.4	-19.3	-19.8	-19.9	-19.2	-19.1
$M_{\text{V,max}}$ / mag	-17.6	-18.8	-19.6	-19.9	-20.1	-20.1	-19.4	-19.4
$M_{\text{R,max}}$ / mag	-18.4	-19.1	-19.4	-19.4	-19.4	-19.2	-19.0	-19.1
$M_{\text{I,max}}$ / mag	-18.9	-19.2	-19.2	-19.4	-19.6	-19.7	-18.9	-19.0
$(U - B)_{\text{Bmax}}$ / mag	0.58	0.41	0.50	0.19	0.08	-0.26	-0.04	0.35
$(B - V)_{\text{Bmax}}$ / mag	1.67	1.51	1.13	0.59	0.28	0.08	0.11	0.30
$(V - R)_{\text{Bmax}}$ / mag	0.74	0.36	-0.13	-0.46	-0.67	-0.82	-0.30	-0.28
$(V - I)_{\text{Bmax}}$ / mag	1.26	0.39	-0.47	-1.05	-1.48	-1.47	-0.64	-0.49

Note. — M_{tot} , M_{core} , and M_{sh} are the masses of the WD, the C/O core, and the helium shell, respectively. All masses are given in units of the solar mass. $\Delta m_{15}(B)$ and $t_{\text{max}}(B)$ refer to the decline parameter and the rise time to maximum light in the angle-averaged B -band light curves, respectively. $M_{\text{B,max}}$, $M_{\text{V,max}}$, $M_{\text{R,max}}$ and $M_{\text{I,max}}$ denote the angle-averaged peak magnitudes at the true peaks in the given bands. Colours are quoted at time $[t_{\text{max}}(B)]$ of B -band maximum.

^a At maximum light ^{56}Ni , ^{52}Fe and ^{48}Cr will have mostly decayed to ^{56}Co , ^{52}Cr and a mixture of ^{48}V and ^{48}Ti , respectively.

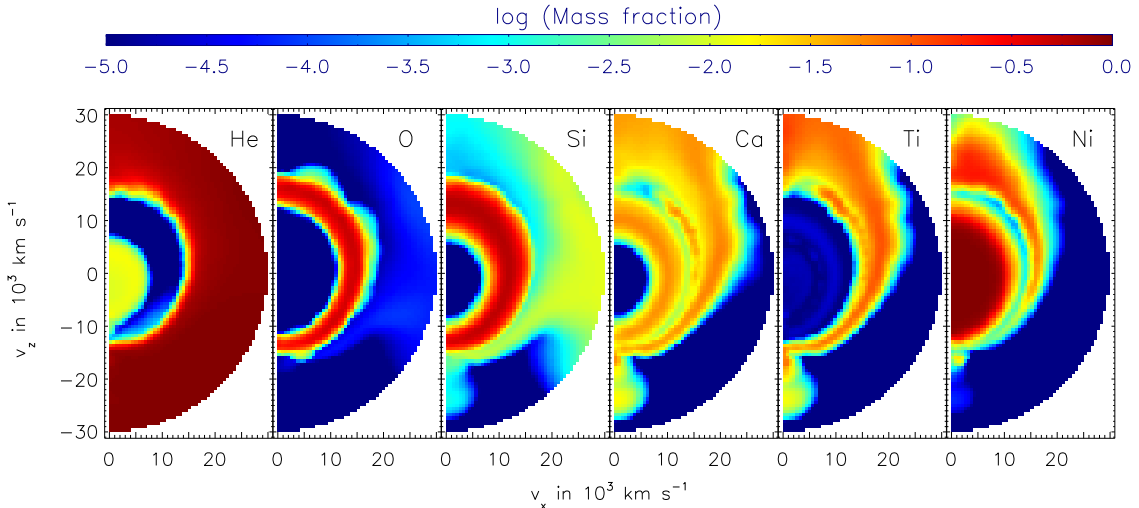


Figure 1. Final composition structure of selected species of Model 3 of Fink et al. (2010). The individual panels show the mass fractions of He, O, Si, Ca, Ti and Ni (from left to right, respectively). The model is radially symmetric about the z -axis.

ing to the initial distribution of ^{56}Ni , ^{52}Fe and ^{48}Cr , as appropriate, and follow the homologous expansion until they decay. Decay times are sampled in a two step process. If the pellet was assigned to the ^{56}Ni chain, for example, we first choose whether it belongs to a decay of the parent nucleus ^{56}Ni or the daughter nucleus ^{56}Co by sampling the probabilities $E_{^{56}\text{Ni}}/(E_{^{56}\text{Ni}} + E_{^{56}\text{Co}})$ and $E_{^{56}\text{Co}}/(E_{^{56}\text{Ni}} + E_{^{56}\text{Co}})$, respectively. Finally an appropriate decay time is sampled

$$t_{\text{decay}}(^{56}\text{Ni}) = -\tau(^{56}\text{Ni}) \log(z_1) \quad (2)$$

$$t_{\text{decay}}(^{56}\text{Co}) = -\tau(^{56}\text{Ni}) \log(z_1) - \tau(^{56}\text{Co}) \log(z_2) \quad (3)$$

from the mean life times of the ^{56}Ni [$\tau(^{56}\text{Ni}) = 8.80$ d] and ^{56}Co [$\tau(^{56}\text{Co}) = 113.7$ d] nuclei. z_i are random numbers between 0 and 1. The ^{52}Fe [$\tau(^{52}\text{Fe}) = 0.4974$ d, $\tau(^{52}\text{Mn}) = 0.02114$ d] and ^{48}Cr [$\tau(^{48}\text{Cr}) = 1.296$ d, $\tau(^{48}\text{V}) = 23.04$ d] chains are treated in the same way.

Upon decay, a pellet transforms to a single γ -packet representing a bundle of monochromatic-radiation of cmf energy ϵ_0 . The cmf photon energy of the γ -packets is randomly sampled from the relative probabilities of the γ -lines in the appropriate decay of the selected decay sequence – including annihilation lines due to positron emission. Following Lucy (2005), we assume that positrons released by radioactive decays annihilate in situ, giving rise to the emission of two 511 keV γ -ray photons. In doing so, we neglect the kinetic energy released by stopping the positrons, any positron escape and possible positronium formation which gives rise to the emission of continuum photons (see discussion by Milne et al. 2004). Thus, our prediction of the 511 keV line flux should be considered as an upper limit. The γ -packets are then propagated through the ejecta as described by Kromer & Sim (2009).

The γ -line data is taken from Table 1 of Ambwani & Sutherland (1988) for the ^{56}Ni decay-sequence and from Burrows (2006) for the ^{48}Cr decay-sequence, respectively. Owing to the comparatively short life times of ^{52}Fe and ^{52}Mn , these nuclei have mostly already decayed to their daughter nuclei when we start the radiative transfer simulation at ~ 1 day. Since the ejecta at these early times are almost opaque to γ -rays, the γ -packets released by the ^{52}Fe decay chain will be thermalized rapidly. Therefore we do not follow the propagation of the γ -packets released by the ^{52}Fe decay chain, but immediately convert their energy to thermal kinetic energy (k -packets in the framework of ARTIS).

The input models (composition, density, velocities) for the radiative transfer simulations were derived using the tracer particles from the hydrodynamics simulations (see Fink et al. 2010 for details on the hydro setup and use of tracer particles for nucleosynthesis). Since the tracer particles are Lagrangian, we use an approach similar to the reconstruction of the density field in smooth particle hydrodynamics (SPH) simulations to construct the input model from the tracers. For the models described here, the density field was obtained using the SPH method described by Dolag & Stasyszyn (2009) (specifically, their equations 1 – 3) adopting $N = 32$ for the SPH smoothing-length normalisation factor. For the

centre (\mathbf{x}_i) of each grid cell (i) in the model, the mass fractions ($X_{Z,i}$) of the elements considered ($Z = 1$ to 30) were reconstructed using

$$X_{Z,i} = \rho_i \sum_j W(|\mathbf{x}_i - \mathbf{x}_j|, h_j) X_{Z,j}, \quad (4)$$

where ρ_i is the reconstructed mass density, $X_{Z,j}$ is the mass-fraction of element Z for tracer particle j (which lies at position \mathbf{x}_j), h_j is the SPH particle smoothing length and $W(x, h)$ the SPH kernel function (defined via equations 3 and 1 of Dolag & Stasyszyn 2009, respectively). The mass fractions of the important radioactive isotopes (^{56}Ni , ^{56}Co , ^{52}Fe and ^{48}Cr) were reconstructed from the tracer particle yields in exactly the same manner. The reconstruction was performed on an 80×160 (r, z)-grid using the final state of the tracer particles at the end of the simulations (which were run up to the phase of homologous expansion).

For the radiative transfer simulation this 2D model is re-mapped to a 3D Cartesian grid of size 100^3 which co-expands with the ejecta. We then follow the radiative transfer from 2 to 120 days after the explosion, discretized into 111 logarithmic time steps each of duration $\Delta \ln(t) = 0.037$. Using our detailed ionization treatment and the cd23_gf-5 atomic data set (Kromer & Sim 2009), we simulated the propagation of 2×10^7 packets. To speed up the initial phase of the calculation we made use of our initial grey approximation for the first 30 time steps (adopting a parameterised grey opacity for the highly optically thick cells in the centre of our simulation volume). The first ten time steps were treated in local thermodynamic equilibrium (LTE).

4. SYNTHETIC OBSERVABLES

In this Section we present synthetic observables for the models of Fink et al. (2010). First we consider angle-averaged ultraviolet, optical and infrared light curves and explore the diversity within this set of models and compare it to that of observed SNe Ia (Section 4.1). Then we investigate the colour evolution and spectra of these models (Sections 4.2 and 4.3). In Section 4.4 we study the effects of the asymmetric ejecta composition. Finally, in Section 4.5, we briefly discuss the γ -ray emission from these models.

4.1. Broad-band light curves

In Figure 2 we show the angle-averaged ultraviolet-optical-infrared (*UVOIR*) bolometric and U , B , V , R , I , J , H , and K band-limited light curves for the model sequence of Fink et al. (2010) as obtained from our radiative transfer simulations. For comparison to observations we included photometric data of SNe 2005cf (Pastorello et al. 2007b), 2004eo (Pastorello et al. 2007a), 2001el (Krisciunas et al. 2003) and 1991bg (Filippenko et al. 1992; Leibundgut et al. 1993) in the figure. While SN 1991bg, the prototypical event of the subluminous 1991bg-like objects, marks the faint end of observed SNe Ia, SNe 2005cf, 2004eo and 2001el are representative of the spectroscopically normal objects.

Since our models form a sequence of increasing ^{56}Ni -mass, the peak brightness of the synthetic light curves

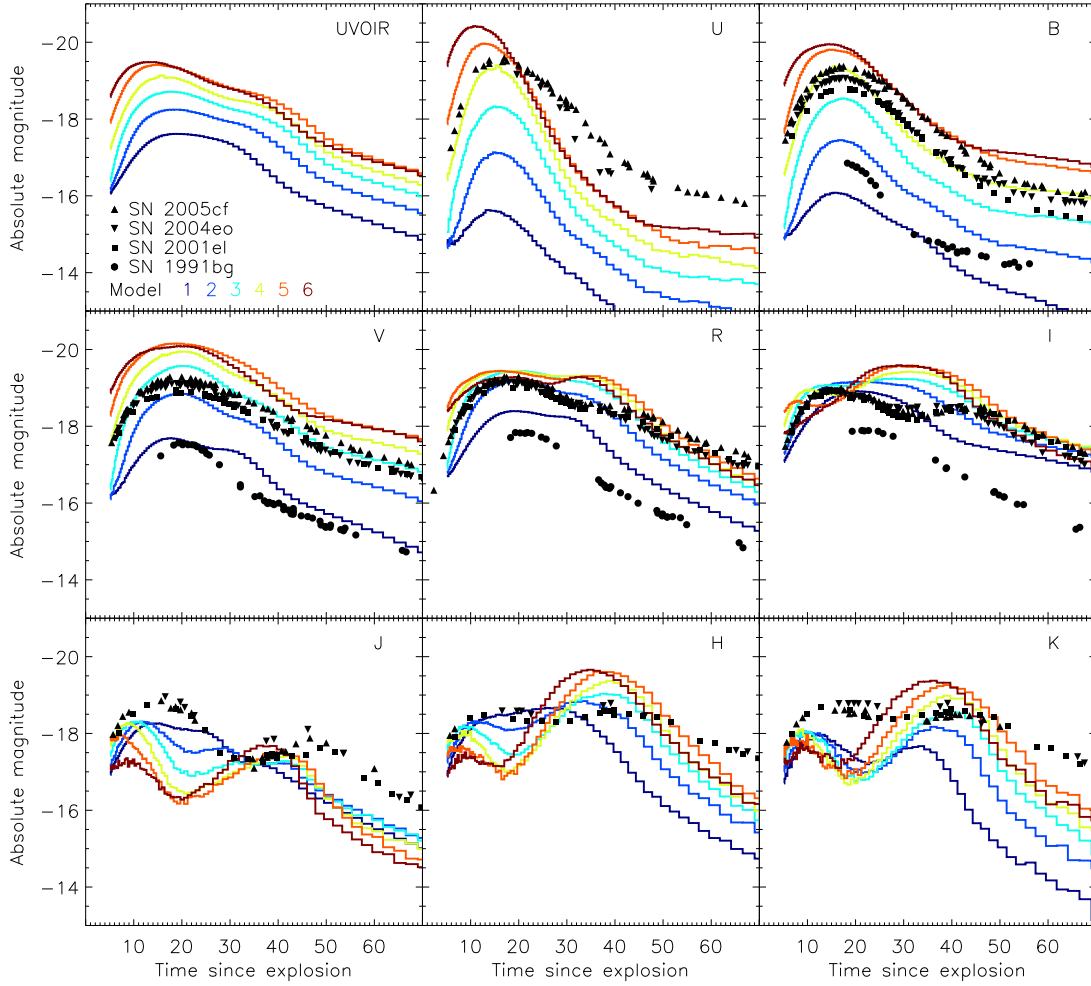


Figure 2. Angle-averaged *UVOIR* bolometric and *U, B, V, R, I, J, H, K* band-limited light curves for the model sequence of Fink et al. (2010) as indicated by the colour coding. For comparison photometrical data of the spectroscopically normal SNe 2005cf (triangles; Pastorello et al. 2007b), 2004eo (upside-down triangles; Pastorello et al. 2007a) and 2001el (squares; Krisciunas et al. 2003) as well as for the subluminal SN 1991bg (circles; Filippenko et al. 1992, Leibundgut et al. 1993) are shown.

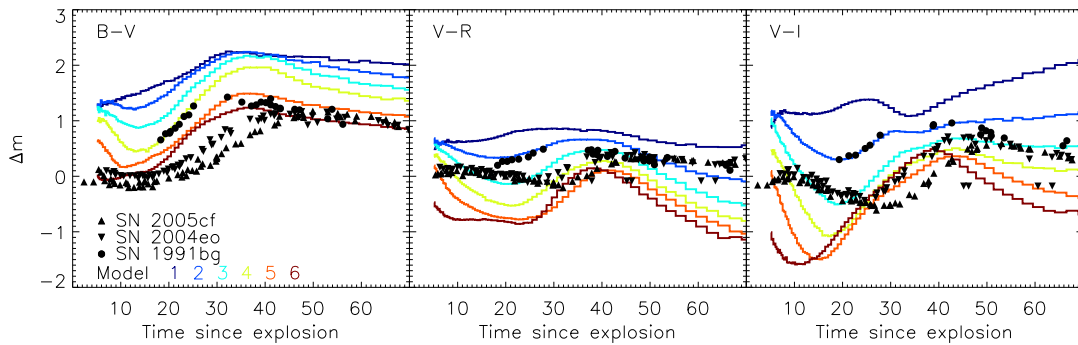


Figure 3. Angle-averaged colour curves of our models as indicated by the labels. The different panels correspond to *B-V*, *V-R* and *V-I* colour (from left to right). For comparison, the colours of the spectroscopically normal SNe 2005cf (triangles; Pastorello et al. 2007b) and 2004eo (upside-down triangles; Pastorello et al. 2007a) as well as for the the subluminal SN 1991bg (circles; Filippenko et al. 1992, Leibundgut et al. 1993) are shown.

increases from Model 1 to Model 6: for B -band maximum, for example, we find a range from -15.9 mag for Model 1 to -19.9 mag for Model 6 (values for the intermediate models and other bands are given in Table 1). This covers almost the full range of peak brightnesses observed among SNe Ia (e.g. Hicken et al. 2009), excluding only the very brightest events like SN 2003fg (Howell et al. 2006) which have been suggested to derive from super-Chandrasekhar-mass progenitor systems (see however Hillebrandt et al. 2007; Sim et al. 2007).

Despite their lower total mass, and thus lower overall opacity, our model light curves do not show particularly fast evolution compared to Chandrasekhar-mass models. In contrast, Höflich & Khokhlov (1996) reported a fast initial rise and broad peaks for their helium detonation models. For the rise times from explosion to B -band maximum [$t_{\max}(B)$] we find values between 17.0 and 17.7 days for our least massive models (1 to 3, cf. Table 1). This is in good agreement with observational findings (e.g. Hayden et al. 2010 find rise times to B -band maximum between 13 and 23 days with an average value of 17.38 ± 0.17 days). In contrast, the more massive Models (4 to 6) show shorter B -band rise times with increasing mass (see Table 1): for Model 6, $t_{\max}(B)$ is only 14.3 days. The peak time is mainly set by the diffusion time for photons to leak out from the ^{56}Ni -rich inner core. Owing to the larger densities in the more massive models, nuclear burning produces ^{56}Ni out to much higher velocities than in the lower mass models (compare Figure 3 of Fink et al. 2010). Moreover, the helium shell masses in our models decrease for the heavier WDs. Thus, the mass (and therefore opacity) on top of the ^{56}Ni -rich inner core decreases with increasing WD mass and photons start to escape earlier for the more massive models making their light curves peak faster (compare also the rise times to bolometric maximum in Fink et al. 2010). In addition, we note that the radioactive nuclides which are produced in the helium shell burning have some influence on the initial rise phase of the light curves (see Figure 8 of Fink et al. 2010).

In the post-maximum decline phase, characterized by the decline parameter $\Delta m_{15}(B)$ which gives the change in B -band magnitude between maximum and 15 days thereafter, our models show a peculiar characteristic. Observationally, brighter SNe Ia show a trend of slower declining light curves (e.g. Phillips 1993; Hicken et al. 2009). In contrast, the model light curves decline faster along our sequence from Model 1 to 4 despite increasing brightness (cf. Table 1).

Specifically, we find $\Delta m_{15}(B) \sim 0.88$ for Model 1, which according to peak brightness would be classified as a subluminescent explosion. However, observationally these events are characterized by a fast decline [$\Delta m_{15}(B) \sim 1.9$, e.g. Garnavich et al. 2004; Taubenberger et al. 2008]. In contrast, Model 4, which has a B -band peak magnitude typical for a spectroscopically normal SN Ia, yields $\Delta m_{15}(B) \sim 1.77$ which is much faster than typically observed [$\Delta m_{15}(B) \sim 1$, e.g. Hicken et al. 2009]. Although $\Delta m_{15}(B)$ is lower for the brighter Models 5 and 6, they still decline too fast compared to observed objects of corresponding brightness. A similar trend for more rapidly declining light curves from more massive models is also seen in the bolometric light curves of Model 2 to 6 (cf. Table 4 of Fink et al. 2010).

In contrast to earlier work by Höflich & Khokhlov (1996), who studied sub-Chandrasekhar-mass models with significantly more massive shells, we do not find particularly fast evolution in the post-maximum decline of our light curves compared to those obtained for other types of models. Applying our radiative transfer code ARTIS for example to the well-known W7 model (Nomoto et al. 1984; Thielemann et al. 1986), which is widely regarded as a good standard for SNe Ia, we find $\Delta m_{15}(B) \sim 1.6$ when using the same atomic data set as adopted here. This value is comparable to our fastest declining sub-Chandrasekhar-mass model and also too fast compared to normal SNe Ia.

In addition, we note that $\Delta m_{15}(B)$ is also quite sensitive to the details of the radiative transfer treatment. Using an atomic data set with 8×10^6 lines (the big_gf-4 data set of Kromer & Sim 2009), for example, yields $\Delta m_{15}(B) \sim 1.75$ for W7. In contrast, a simulation using the atomic data set adopted in this study but applying a pure LTE treatment for the excitation/ionization state of the plasma yields $\Delta m_{15}(B) \sim 1.95$ for W7. This shows that systematic uncertainties in the radiative transfer treatment can affect $\Delta m_{15}(B)$ by several tenths of a magnitude (see also the comparison of different radiative transfer codes in Figure 7 of Kromer & Sim 2009). Thus, we argue that there is no evidence that our sub-Chandrasekhar-mass models fade too fast compared to other explosion models.

4.2. Colour evolution

The most striking difference between our light curves and those of the comparison objects in Figure 2 concerns their colour. To highlight this we show the angle-averaged time-evolution of the $B - V$, $V - R$ and $V - I$ colours for all our models in Figure 3 and compare them again to our fiducial SNe 2005cf, 2004eo, 2001el and 1991bg.

In $B - V$ all our models show positive colour indices for the whole simulation period and a red peak at ~ 40 days after explosion. Contrary to observed SNe Ia (Lira 1995), however, we find no convergence of the different models at epochs after the red peak. Instead, our models at all times form a sequence of increasingly redder $B - V$ colour towards the fainter explosions. With the exception of Model 6, all our models are generally too red compared to spectroscopically normal SNe Ia. At maximum light, for example, we find $(B - V)$ -values of 1.67 and 0.28 for Model 1 and Model 5, respectively (values for the other models are given in Table 1). In contrast, spectroscopically normal SNe Ia are characterized by $(B - V)_{\max} \sim 0.0$ mag.

Subluminescent 1991bg-like objects show a redder $B - V$ colour before the red peak, reaching $B - V \sim 0.4 \dots 0.7$ mag at B -band maximum (Taubenberger et al. 2008). Although Model 4 can reproduce this, it is not a good fit to 1991bg-like objects, since it is considerably too bright (compare Figure 2). Our subluminescent Models 1 and 2, on the other hand, are significantly redder than observed ($B - V$ colours of 1.67 and 1.51 at maximum, respectively). In contrast, Höflich & Khokhlov (1996) and Höflich et al. (1996) found too blue colours at maximum light for their subluminescent sub-Chandrasekhar-mass models compared to 1991bg-like objects.

The origin of our red colours traces back to the ex-

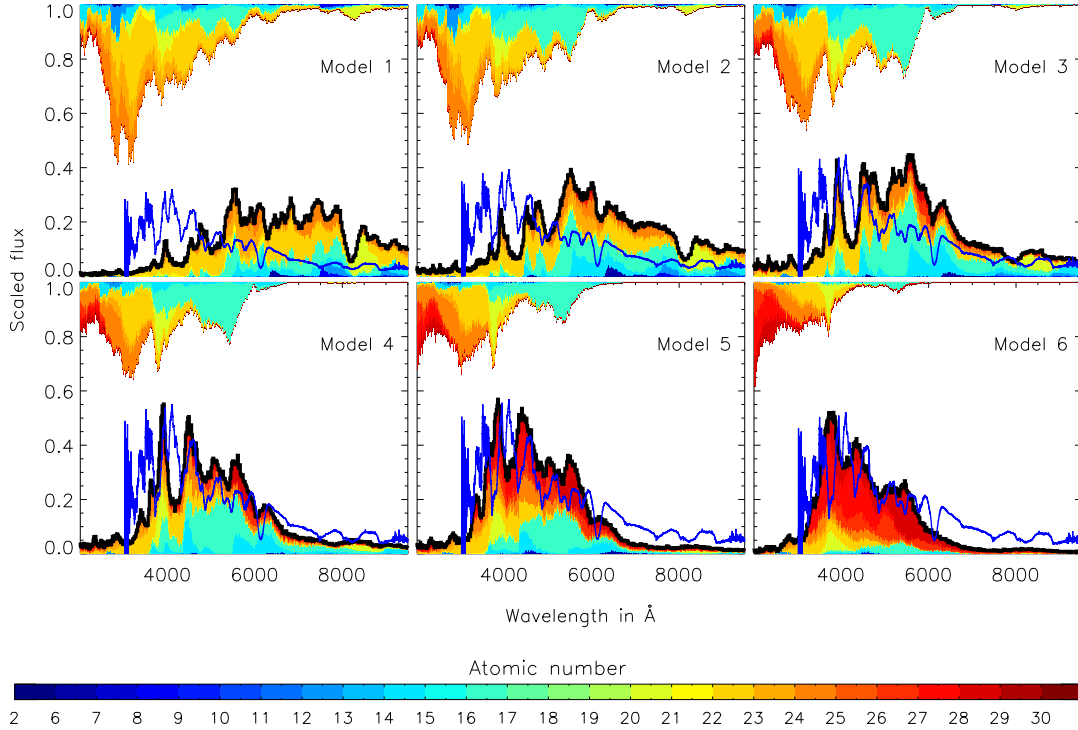


Figure 4. Angle-averaged (thick black line) spectra at three days before B -band maximum for all six of our models as indicated by the labels. For comparison the blue line shows the de-redshifted and de-reddened spectrum of SN 2004eo (Pastorello et al. 2007a) at the corresponding epoch. This was scaled such that its maximum matches the maximum of the model spectrum. The colour coding indicates the element(s) responsible for both bound-bound emission and absorption of quanta in the Monte Carlo simulation. The region below the synthetic spectrum is colour coded to indicate the fraction of escaping quanta in each wavelength bin which last interacted with a particular element (the associated atomic numbers are illustrated in the colour bar). Similarly, the coloured regions above the spectra indicate which elements were last responsible for removing quanta from the wavelength bin (either by absorption or scattering/fluorescence).

tended layer of titanium and chromium which is present in the helium shell ejecta of our models. This will be discussed in more detail in Section 4.3.

While the trend of increasingly redder colours for fainter models persists in the $V - R$ index, our models are not systematically too red here. Model 2 and 3 populate about the right range for 1991bg-like and spectroscopically normal SNe Ia, respectively. However, the details of their $V - R$ evolution, especially the initial decline present in all the models, do not match the observations.

A similar behaviour is found for the $V - I$ colour where again Model 2 and 3 lie closest to the observed colours of 1991bg-like and spectroscopically normal SNe Ia, respectively. However, again the agreement is imperfect. For Model 2 this is most obvious at the latest epochs, where 1991bg-like objects start to become bluer while the model colour maintains a redward evolution. Moreover, the model shows a secondary blue minimum, due to the post-maximum plateau of the V -band light curve which is not observed in 1991bg-like objects. In Model 3 the initial decline and the rise to the red peak are significantly different from the observed behaviour of spectroscopically normal SNe Ia.

4.3. Spectra

The properties of our model light curves can be understood from consideration of the synthetic spectra. Figure 4 shows the angle-averaged spectrum of all our models at three days before B -band maximum. For comparison, we also show the spectrum of SN 2004eo

(Pastorello et al. 2007a) at the corresponding epoch. The colour coding below the synthetic spectrum indicates the fraction of escaping quanta in each wavelength bin which were last emitted in bound-bound transitions of a particular element. Similarly, the coloured regions above the spectra indicate which elements were last responsible for removing quanta from a wavelength bin by bound-bound absorption. This coding allows us to both identify individual spectral features and track the effect of fluorescence on the spectrum formation directly. The contributions of bound-free and free-free emissions to the total flux are so small that they are not discernable in the figure.

From this it is immediately obvious that the colours of our models are due to fluorescence in titanium and chromium lines. Having a wealth of strong lines in the UV and blue, even small amounts of these elements effectively block radiation in the UV and blue and redistribute it to redder wavelengths where the optical depths are smaller and the radiation can escape. Compared to other explosion models, this effect is particularly strong in the Fink et al. (2010) models, since they produce relatively large amounts of titanium and chromium in the outer layers during the initial helium detonation (cf. Table 1 and Figure 1; typical titanium and chromium yields for other explosion models are on the order of the yields from the core detonation). This also explains the trend for redder colours in the fainter models: according to Table 1, the production of titanium and chromium in the

shell increases continuously from Model 6 to Model 1.

Since this titanium and chromium layer is located at higher velocities than most of the intermediate mass elements (cf. Figure 1), redistribution by titanium and chromium also dilutes the absorption features of intermediate-mass elements like silicon and sulphur by reprocessing flux into the relevant wavelength regions. This can be clearly seen in Figure 4. Although Models 1 and 2 produce the largest amounts of silicon of all our models (0.27 and 0.25 solar masses in the core, respectively), they show only a (very) weak Si II $\lambda 6355$ feature since this wavelength region is strongly polluted by flux redistribution from titanium and chromium. The only feature of intermediate-mass elements which is clearly visible in these models is the Ca II near-infrared (NIR) triplet at $\lambda\lambda 8498, 8542, 8662$. This feature remains unburied since calcium exists co-spatially with titanium and chromium in the outer shell (Figure 1).

Of all our models, Model 3 [$M_{\text{core}}(^{28}\text{Si}) = 0.21 M_{\odot}$] produces the strongest Si II $\lambda 6355$ feature. For more massive models the silicon yields from the core detonation drop dramatically since, owing to the higher densities, a larger fraction of the core is burned to iron-group elements (see Table 1 and Figure 3 of Fink et al. 2010). As expected from studies of pure detonations of Chandrasekhar-mass WDs (Arnett et al. 1971), the extreme case of Model 6 (almost the Chandrasekhar mass) produces no significant amounts of intermediate-mass elements. Thus the spectrum is totally dominated by iron-group elements. Since it shows no indication of any Si II $\lambda 6355$ feature, this model would not be classified as a SN Ia.

Since none of our models give a good match to the colours and line strengths of observed SNe Ia, we will not discuss line velocities in detail. We note, however, that along the sequence from Model 1 to 5 there is a trend for higher line velocities of intermediate mass elements. This is obvious in the Si II $\lambda 6355$ feature of our models which is apparent in Figure 4. Along the model sequence (1 to 5), this line moves to shorter wavelengths compared to the observed Si II absorption feature of SN 2004eo. This arises because the inner boundary of the region rich in intermediate-mass elements moves to higher velocities with increasing mass due to the more complete burning in the inner regions (compare Figure 3 of Fink et al. 2010).

Finally, we note that none of our model spectra show any indication of helium lines, despite our models having up to $\sim 0.08 M_{\odot}$ of helium in their outer layers (cf. Table 1). Since helium has rather highly excited levels, this might simply be a consequence of our approximate treatment of the plasma state which neglects non-thermal excitation and ionization. We note, however, that despite using the PHOENIX code which does include a treatment of non-thermal processes, Nugent et al. (1997) also found no strong evidence of helium lines for models with even more ($0.2 M_{\odot}$) helium in the outer shell.

4.4. Line-of-sight dependence

As discussed in Section 2, our models show strong ejecta asymmetries due to their ignition in a single-point at the north pole of the WD (cf. Figure 1). These asymmetries are expected to have some influence on the observables along different lines-of-sight. Since they are characteristically the same for all our models, we first

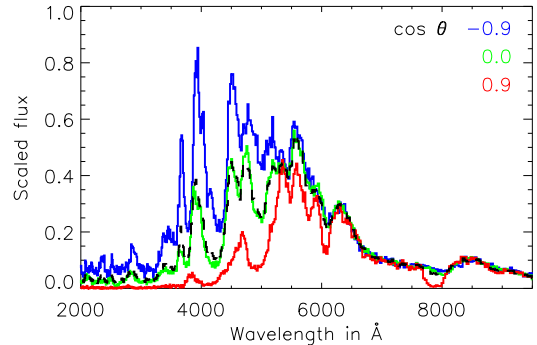


Figure 5. Line-of-sight dependent maximum-light spectra for Model 3. To indicate the maximal effect spectra seen pole-on are plotted and compared to a spectrum seen equator on. The corresponding lines are identified by the colour coding. For comparison the angle-averaged spectrum is shown as the dashed black line.

use Model 3 as an example to give a detailed discussion of line-of-sight dependent spectra and light curves of this model (Sections 4.4.1 and 4.4.2). In Section 4.4.3 we then present the variations in peak magnitudes and colours due to line-of-sight effects for all our models.

4.4.1. Spectra

To obtain line-of-sight dependent observables we bin the escaping photons into a grid of ten equal solid-angle bins in $\mu = \cos \theta$ with θ being the angle between the line-of-sight and the z -axis of the model. In Figure 5 we show the maximum-light spectra of Model 3 for three different directions, corresponding to lines-of-sight close to the southern polar axis ($\mu = -0.9$), the northern polar axis ($\mu = 0.9$) and equator-on (average of the $\mu = -0.1$ and 0.1 bins). While the equator-on spectrum looks similar to the angle-averaged spectrum, the spectra seen from the polar directions are significantly different from each other as well as from the angle-averaged spectrum. For $\mu = 0.9$, an observer is looking through the extended layer of iron-group elements in the outer shell of the northern-hemisphere (cf. Figure 1). This blocks almost all the flux in the UV and blue wavelength range and the redistribution of this flux leads to a very red spectrum. In contrast, this layer of iron-group elements in the outer shell is far less extended on the southern hemisphere, where the shell burning is less efficient. Thus, an observer with $\mu = -0.9$ sees a bluer spectrum than equator-on. Equator-on the extension of the layer of iron-group elements is somewhere between these two extremes and the spectrum resembles the angle-averaged case.

A secondary effect results from the off-centre ignition of the core. Since the core has been compressed less strongly on the northern hemisphere, the core detonation yields more intermediate-mass elements on the northern than on the southern hemisphere (cf. Figure 1 and the Discussion in Section 4.3 of Fink et al. 2010). This leads to stronger features of intermediate-mass elements in the spectrum seen along the northern polar-axis and becomes particularly visible in the strength of the Si II 6355 Å feature and the Ca II NIR-triplet which become weaker from $\mu = 0.9 \rightarrow -0.9$.

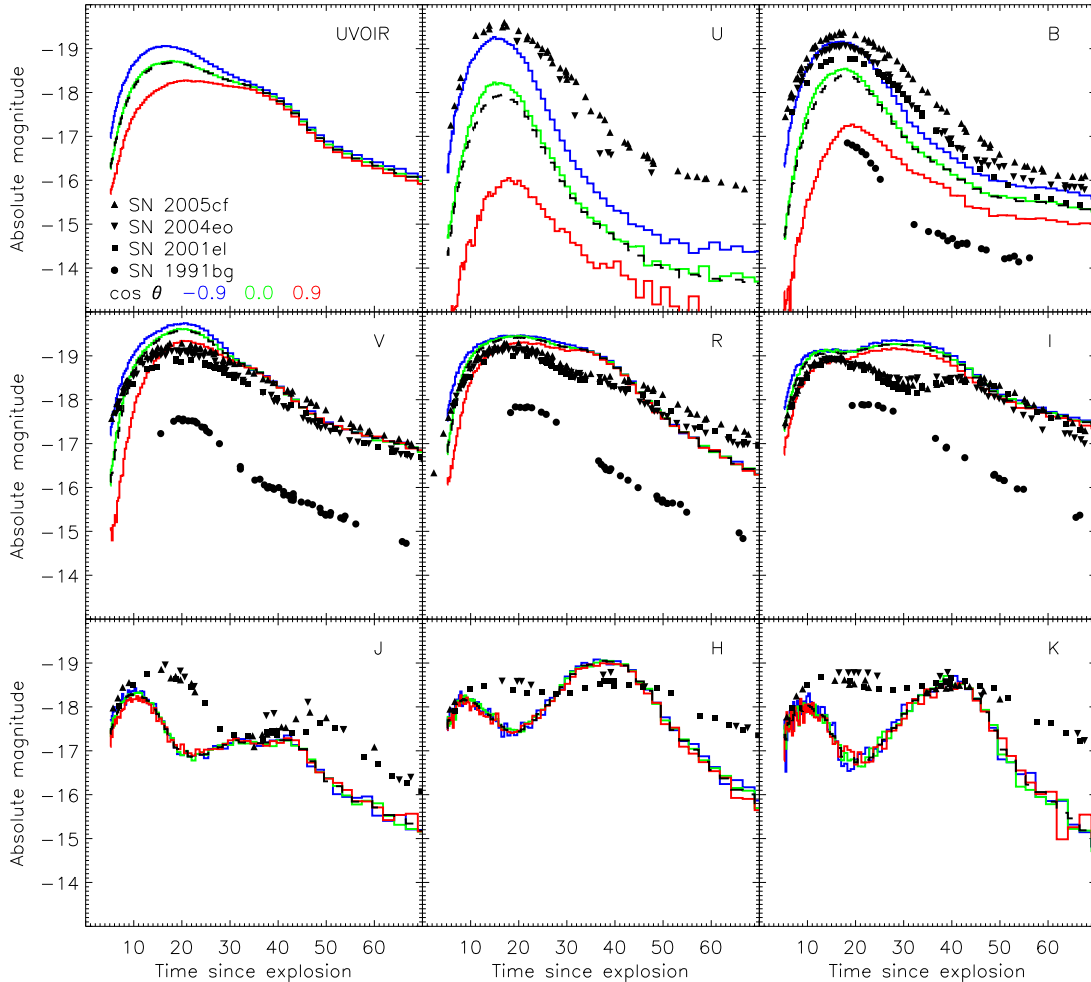


Figure 6. Selected line-of-sight dependent light curves of Model 3 as indicated by the colour coding. For comparison angle-averaged light curves (black dashed) and photometrical data of our fiducial SNe 2005cf, 2004eo, 2001el and 1991bg (different symbols) are shown.

4.4.2. Lightcurves

Figure 6 shows band-limited synthetic light curves from our radiative transfer simulations for Model 3 as seen equator-on and from the two polar directions. As already noted for the maximum-light spectra, our model shows a trend for increasingly red colours from $\mu = -0.9 \rightarrow 0.9$. Similarly, we find a clear dependence of the light curve rise and decline times on the line-of-sight. While the rise times increase along the sequence $\mu = -0.9 \rightarrow 0.9$ (for B band, for example, we find rise times between 16.8 and 19.7 days for $\mu = -0.9$ and $\mu = 0.9$, respectively), the light curve declines more slowly [$\Delta m_{15}(B) = 1.91$ and $\Delta m_{15}(B) = 1.29$ for $\mu = -0.9$ and $\mu = 0.9$, respectively]. Moreover, we find a clear trend for a weaker dependence of the light curves on the line-of-sight at lower photon energies. Thus, while U and B band show a variation of ~ 3 and ~ 2 magnitudes at maximum light, respectively, the variation in V band is already less than half a magnitude and in the NIR bands there is virtually no viewing-angle effect.

All these effects are due to the asymmetry of the layer of iron-group elements in the outer shell. Since this layer is more extended on the northern hemisphere it causes additional line blocking and thus enhanced fluorescence

and photon trapping for inclinations close to $\mu = 1$. This explains the redder colours as well as the increasing rise and decreasing decline times for $\mu = -0.9 \rightarrow 0.9$. For lower photon energies, the asymmetry of the outer shell is less important, since the optical depths are smaller and photons typically escape from deeper layers of the ejecta. In the NIR bands the entire ejecta contribute to the emitted photons and the viewing-angle dependence of the light curves is very small.

This is illustrated in Figure 7 which shows where photons of selected bands were last emitted before they escaped from the supernova ejecta at different times. While U -band photons leak out predominantly from the regions on the southern hemisphere, where the layer of iron-group elements is least extended, I -band photons show no strong preference for a particular region. In fact, even before maximum light the whole ejecta contribute to I -band emission. V -band photons, in contrast, show some preference for leaking out from the southern hemisphere before and immediately after maximum light. From about 10 days after maximum light this preference disappears. This is directly reflected in the V -band light curve in Figure 6 which becomes viewing-angle independent at about that time.

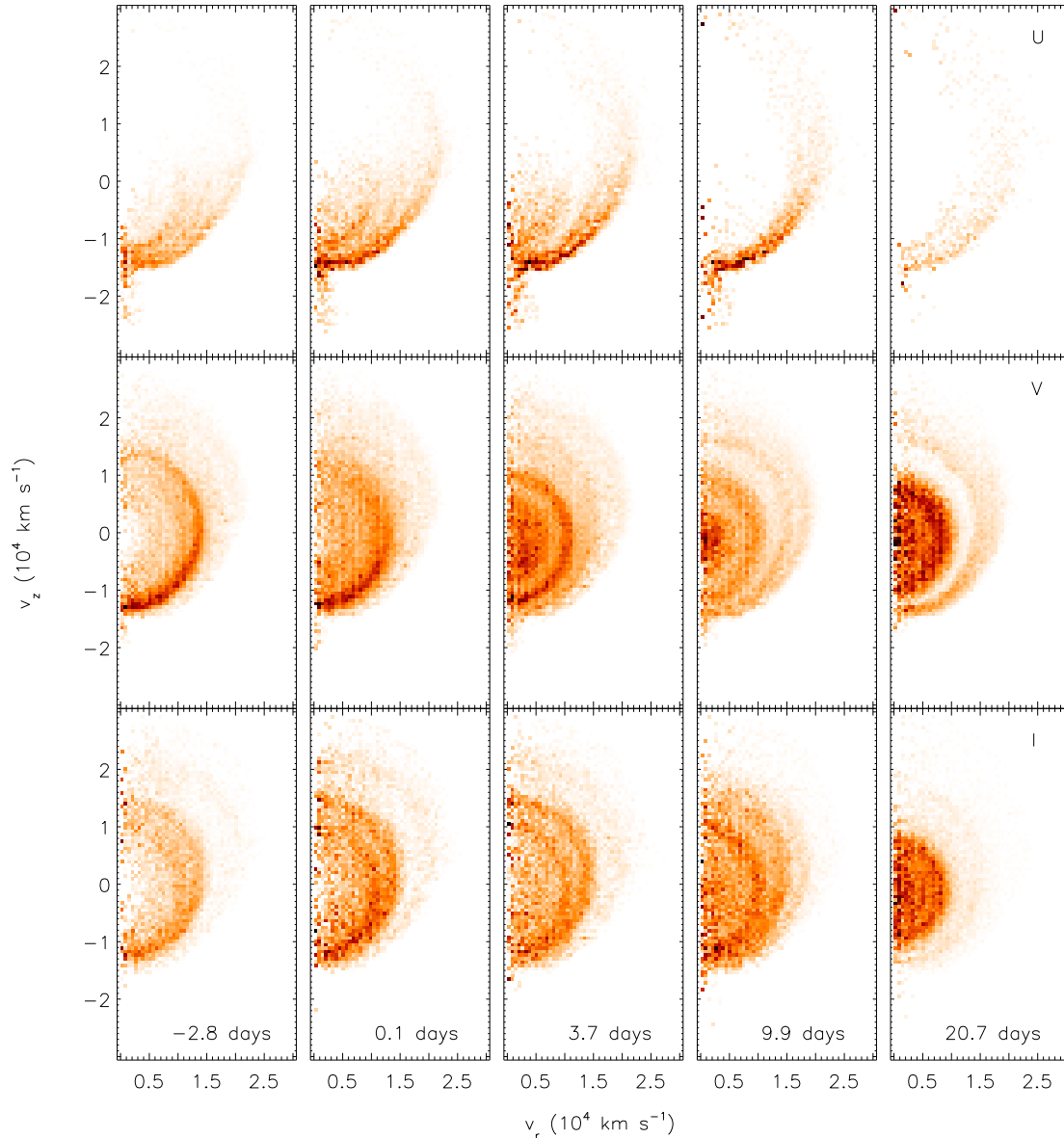


Figure 7. Region of last emission for selected bands (U , V , I from top to bottom) and different times (from left to right). The epochs indicated in the bottom panels are given in days with respect to B -band maximum. Dark regions contribute most to the flux escaping in the band. The model is symmetric under rotation about the z -axis.

Finally, we note that the strong line-of-sight dependence of our synthetic observables poses an additional problem for the Fink et al. (2010) models. Even if some particular line-of-sight might compare more favourably to observed SNe Ia than others (as does for example the southern line-of-sight for the light curves in Figure 6), all lines-of-sight should occur in nature – including the most peculiar ones. Moreover, the large dispersion in brightness at B -band maximum which we find in our model is in conflict with observations.

4.4.3. Other models

Since the other models in the Fink et al. (2010) sequence have the same characteristic asymmetries, their light curves and spectra show a similar viewing-angle dependence. However, the strength of this viewing-angle dependence varies between the models, due to their dif-

ferent helium shell masses. To demonstrate this, Figure 8 shows selected light curve properties of all models for the ten different viewing directions within our uniform grid in μ .

As expected, the viewing-angle dependence decreases for smaller helium shell mass. Thus, we find a scatter of more than 2 magnitudes for the brightness at B -band maximum between the different lines-of-sight in Model 1 and 2, while Model 6 shows only a scatter of ~ 0.3 magnitudes. Similar trends can be observed for the $B-V$ and $V-R$ colours at B -band maximum. While Model 6 shows almost no dependence on the line-of-sight, the less massive models show a very clear trend for redder colours towards $\mu = 0.9$ (as discussed for Model 3 in detail above).

For the rise times the situation is similar: while Models

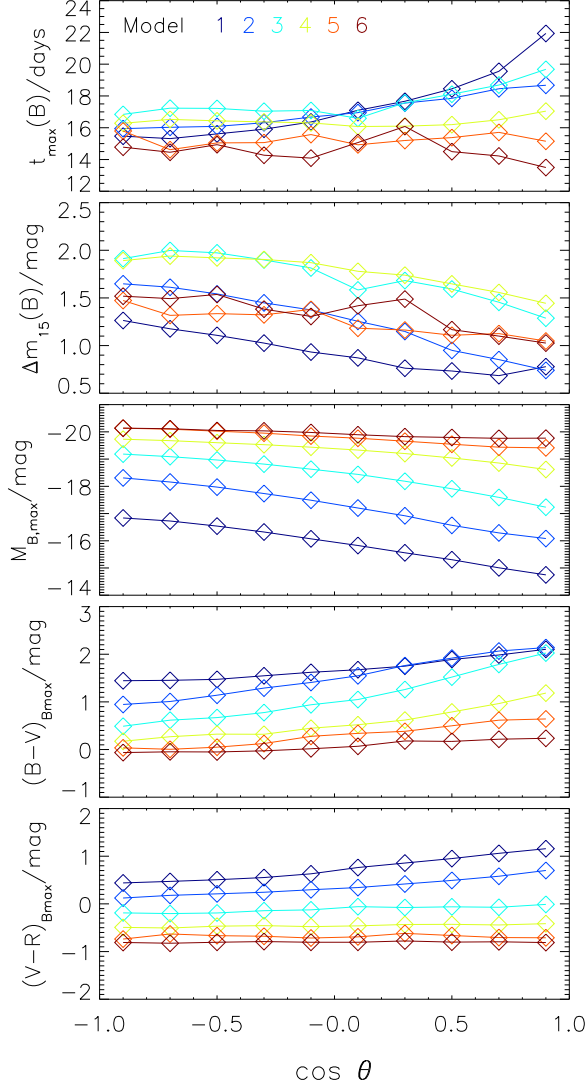


Figure 8. Light curve properties of the Fink et al. (2010) models for 10 different viewing directions (different models are indicated by the colour coding). From top to bottom the panels show the rise-time to B -band maximum [$t_{\max}(B)$], the decline in B -band between maximum light and 15 days thereafter [$\Delta m_{15}(B)$], the B -band peak magnitude ($M_{B,\max}$), the $B - V$ colour at B -band maximum [$(B - V)_{B,\max}$] and the $V - R$ colour at B -band maximum [$(V - R)_{B,\max}$], respectively. The lines connecting the different data points are just to guide the eye.

1, 2 and 3 (relatively massive shells) show a clear trend for increasing B -band rise times from $\mu = -0.9$ to $\mu = 0.9$ due to the enhanced photon trapping by optically thick lines of iron-group elements, we do not observe a clear trend for Models 4, 5, and 6 (less massive shells). Recall, that the average rise times increase from Model 1 to 3, while Models 4 to 6 form a sequence of decreasing rise times. This was already discussed in Section 4.1.

The enhanced trapping of photons by the iron-group layer of the northern hemisphere also affects the post-maximum decline rate in B band. Thus, we find decreasing values of $\Delta m_{15}(B)$ from $\mu = -0.9$ to $\mu = 0.9$. This trend persists for all our models, although it is weaker for the models with the least massive shells.

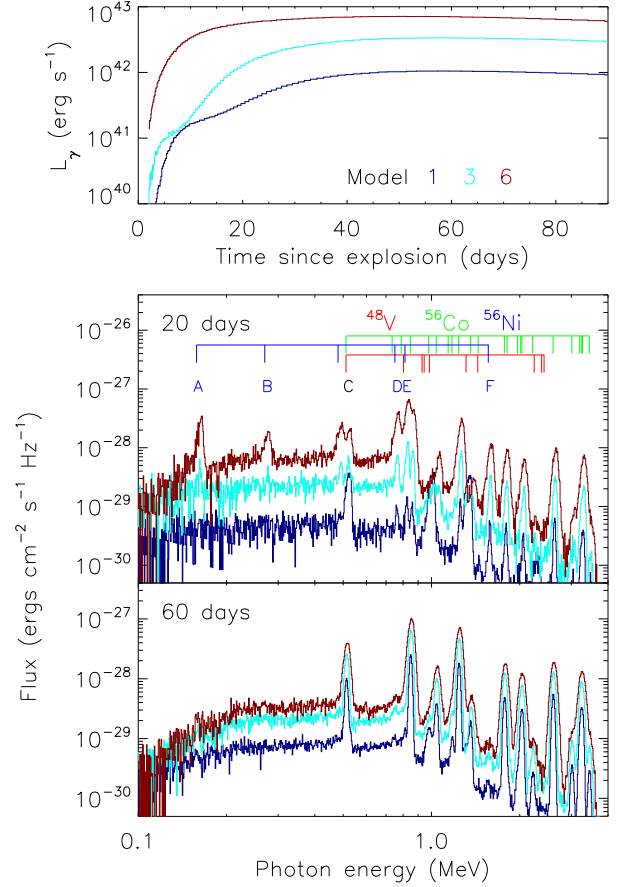


Figure 9. γ -ray light curves (top panel) and spectra (lower panels) for Models 1, 3 and 6 of Fink et al. (2010) as indicated by the colour coding. The spectra shown are for two different epochs which correspond roughly to maximum light in B band (20 days, middle panel) and in γ -rays (60 days, bottom panel). Line features discussed in the text are identified by labels (A – F) in the middle panel (for their identification, see Table 2). In addition, the ^{56}Ni , ^{56}Co and ^{48}V line systems are indicated. The line systems of ^{48}Cr , ^{52}Fe and ^{52}Mn are omitted, since their life times are sufficiently short that these nuclei have already decayed at the shown epochs. Note that at 20 days the line features in the spectra are generally offset towards higher energies compared to the line identifications, due to blue-shifted emission. At 60 days the emission comes from regions of lower velocity and the offset disappears.

4.5. γ -ray emission

Due to their peculiar composition including a mixture of the radioactive isotopes ^{56}Ni , ^{52}Fe and ^{48}Cr close to the surface, γ -observations might provide an additional discriminant between our sub-Chandrasekhar-mass models and more standard explosion models which do not show radioactive isotopes close to the surface. To investigate this, Figure 9 shows γ -ray light curves and spectra for Models 1, 3 and 6 of our sequence. Line identifications are given for some important features in Table 2.

Broadly speaking, our γ -ray spectra are not dramatically different from those obtained by Sim & Mazzali (2008) for parameterised Chandrasekhar-mass models: they are dominated by strong emission lines, mainly due to ^{56}Co , and a continuum which results from Compton scattering of line photons.

Models 1 and 3 have characteristically similar γ -ray light curves. After an initially fast rise (lasting for about

Table 2
Identification of γ -lines in Figure 9.

Identifier	Photon energy (MeV)	Source
A	0.158	^{56}Ni
B	0.270	^{56}Ni
C	0.511	Annihilation of positrons from ^{56}Co and ^{48}V
D	0.750	^{56}Ni
E	0.812	^{56}Ni
F	1.562	^{56}Ni

5 and 10 days after the explosion for Model 3 and 1, respectively) their light curves have a small plateau before passing to a second rise to maximum light at about 60 days. In contrast, Model 6 shows no early rise/plateau but reaches maximum at about 60 days in one continuous rise. These differences result from the significantly different masses of the helium shells of the models. Model 1 has a rather massive shell of $0.126 M_{\odot}$ with $\sim 0.02 M_{\odot}$ of radioactive isotopes. The fast initial rise of the light curve of Model 1 is caused by γ -photons which originate from this outer shell. Due to the small optical depth in the outer shell, those γ -photons start to stream freely at about 10 days and the emerging flux from the outer shell decreases. At the same time, however, γ -photons from the C/O core start to escape and keep the light curve rising until the core also becomes transparent to γ -rays at about 60 days after which the γ -photons start to stream freely.

For Model 3, we observe the same effect. However, due to its lower helium shell mass ($M_{\text{sh}} = 0.055 M_{\odot}$) γ -photons from the shell escape even earlier (at about 5 days). Since the detonation of the C/O core of this model produces much more ^{56}Ni , the ^{56}Ni -rich region is far more extended than in Model 1. This means that ^{56}Ni nuclei from the C/O core are present in regions where the Compton optical depth is relatively low, allowing their γ -photons to more easily escape. Thus, photons from the core dominate the rise earlier than in Model 1. In the extreme limit of Model 6, the shell ($M_{\text{sh}} = 0.0035 M_{\odot}$) is completely negligible and the massive ^{56}Ni region in the C/O core extends so close to the surface that the rise of the light curve is totally dominated by γ -photons escaping from the C/O core.

A similar effect shows up in the early-time (20 days) γ -ray spectra of our models. While Model 6 shows a clear indication of the 0.158 and 0.270 MeV lines of ^{56}Ni , those are invisible for Model 1. Since the Compton cross-section increases with decreasing photon energy, soft-energy lines are most easily buried by photons being Compton down-scattered from higher energies and can only be observed if ^{56}Ni is present at low optical depths (Gómez-Gomar et al. 1998). Thus the presence of the 0.158 and 0.270 MeV lines of ^{56}Ni in Model 6 is a direct consequence of the large extension of the ^{56}Ni bubble in this model, compared to Model 1. The harder ^{56}Ni lines at 0.750, 0.812 and 1.562 MeV, in contrast, are also visible in Model 1. However, they are weaker due to the smaller mass of ^{56}Ni synthesized in Model 1. Note that despite containing ^{48}Cr or ^{48}V close to the surface, our models show no clear features of these radioactive isotopes in their γ -ray spectra.

An interesting effect concerns the 511 keV annihilation line: for Model 3 and 6 the strength of this line increases from 20 to 60 days significantly, but it does not for Model 1. In Model 1, the 511 keV line is dominated by positrons from ^{48}V at 20 days. Being located in the outer layers, the annihilation photons escape easily making the line strong. At 60 days most of the ^{48}V has already decayed. Then, the 511 keV line results from the annihilation of ^{56}Co positrons from the C/O core. For Model 3 and 6, in contrast, the line is always dominated by annihilation photons originating from ^{56}Co positrons in the C/O core. Due to the longer life time of ^{56}Co and the longer time it takes for photons to escape from the core, the strength of the 511 keV line increases from 20 to 60 days.

5. DISCUSSION

In the last Section we presented synthetic observables for the sub-Chandrasekhar-mass double detonation models with minimum helium shell mass of Fink et al. (2010). Compared to observed SNe Ia, these models show some promising features:

1. They predict a wide range of brightnesses that covers the whole range of observed SNe Ia.
2. Their light curve rise and decline times are for most bands in reasonable agreement with those observed.

But despite these positive features the Fink et al. (2010) models cannot account for all the properties of observed SNe Ia since they have peculiar light curves and spectra:

1. The colours of the models are too red compared to observed SNe Ia. This is particularly obvious in the evolution of the $B - V$ colour, where all the models are redder than spectroscopically normal SNe Ia for all epochs.
2. The model spectra cannot reproduce the strong features of intermediate-mass elements typical of SNe Ia at maximum light.

In detail, there are further problems concerning the exact light curve shapes and decline rates as well as a strong viewing-angle dependence which is caused by the point-like ignition of our models.

We have argued that all these problems are mainly due to the burning products of the helium shell. Moreover, Sim et al. (2010), have recently shown that detonations of centrally ignited spherically symmetric naked sub-Chandrasekhar-mass C/O WDs are capable of reproducing the observed diversity of light curves and spectra

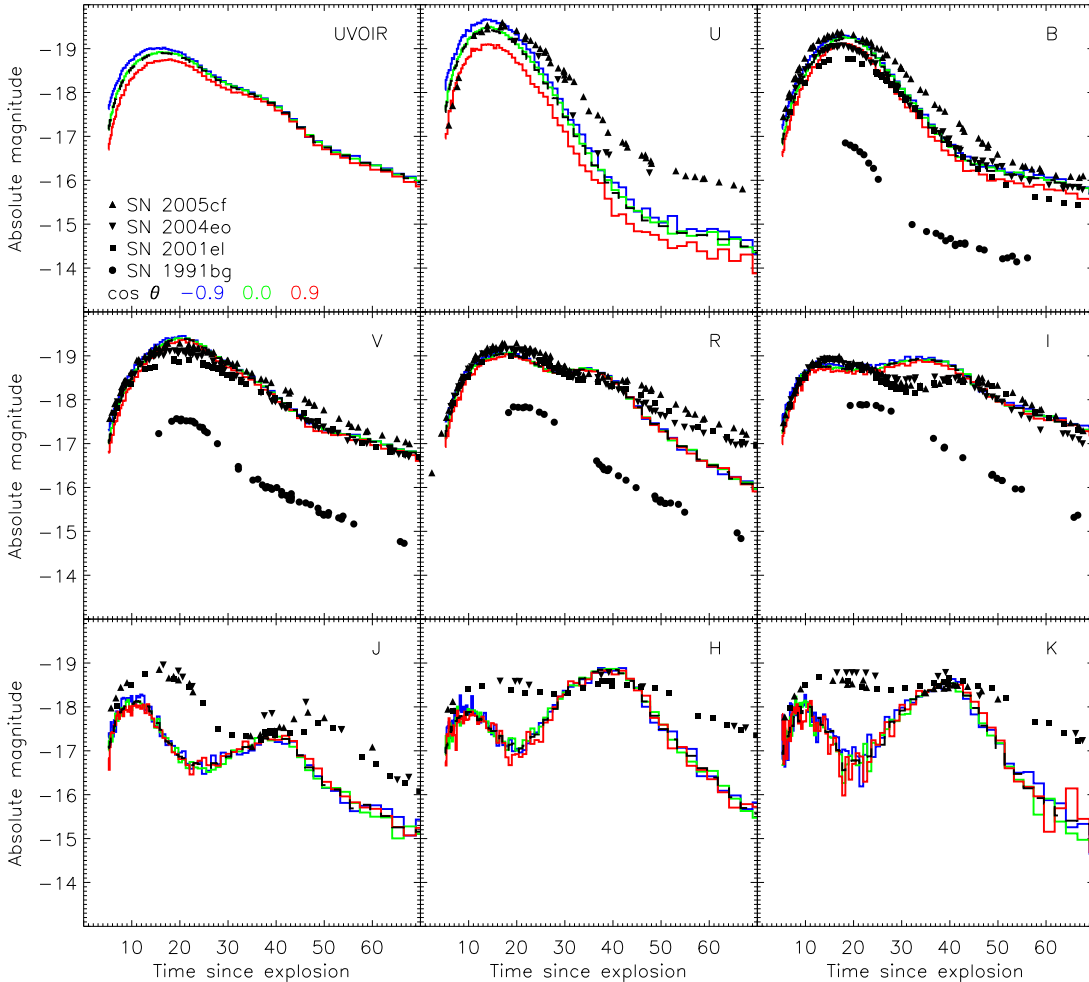


Figure 10. Selected line-of-sight dependent light curves of Model 3c as indicated by the colour coding. For comparison angle-averaged light curves (black dashed) and photometric data of our fiducial SNe 2005cf, 2004eo, 2001el and 1991bg (different symbols) are shown.

of SNe Ia – at least to a similar level of agreement as models of the more standard Chandrasekhar-mass delayed detonations. This naturally leads us to speculate on whether the helium shell in double detonation models could be altered in some way to reduce its negative impact on the synthetic observables.

5.1. Influence of the helium shell

We first explicitly investigate the extent to which the shortcomings and viewing-angle dependence of our models can indeed be attributed to the helium shell. For that purpose we constructed (for Model 3) a toy model which contains only the burning products of the detonation in the initial C/O core but not those of the initial helium shell. For the models of Fink et al. (2010) this can be done in a straightforward manner: since the models use two different sets of tracer particles to simulate the nucleosynthetic yields of core and shell burning respectively (see Section 3.3 of Fink et al. 2010), we obtain such a model by restricting our SPH-like reconstruction algorithm (Section 3) to the core tracers. Properties of this “core-only” model (hereafter 3c) are listed in Table 1.

Figure 10 shows band-limited synthetic light curves obtained from our radiative transfer simulations for this

model as seen equator-on and from the two polar directions. In contrast to the light curves of Model 3 in Figure 6, which are strongly dependent on the viewing angle, the light curves of Model 3c show only a moderate line-of-sight dependence. Thus, at maximum light we find now only a variation of ~ 0.5 and ~ 0.2 magnitudes for U and B band, respectively. For Model 3 these values were significantly larger (~ 3 and ~ 2 magnitudes, respectively). Redder bands show no significant line-of-sight dependence in Model 3c.

Moreover, the light curves of Model 3c give an excellent representation of SN 2004eo in the B , V and R bands. U and I are not in perfect agreement, but still reasonable compared to the agreement between other first principles explosion models and observed SNe Ia (e.g. Kasen et al. 2009). In particular, the colours of this toy model are now in good agreement with observed SNe Ia and not too red as it is the case for Model 3. In the NIR bands, in contrast, the agreement is no better. However, the NIR light curves are much more difficult to model accurately since they require simulations with an extensive atomic data set to properly simulate flux redistribution by fluorescence which strongly affects these bands (Kasen 2006; Kromer & Sim 2009). Here, however, we

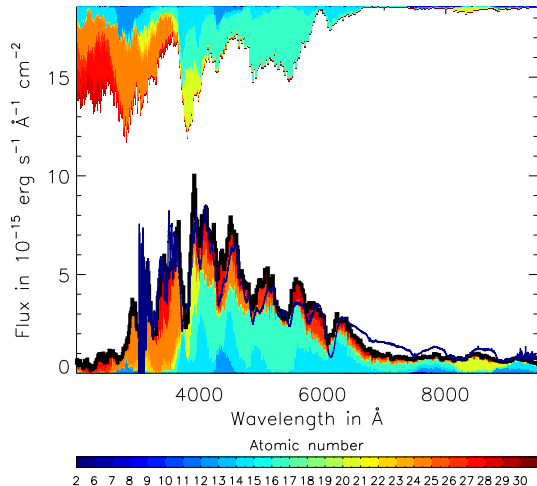


Figure 11. Angle-averaged (thick black line) spectra at three days before B -band maximum for Model 3c. For comparison the blue line shows the de-redshifted and de-reddened spectrum of SN 2004eo (Pastorello et al. 2007a) at the corresponding epoch. Note, that the flux is here in physical units and not scaled like in Figure 4. For a description of the colour coding see Figure 4.

have restricted ourselves for computational reasons to a simplified atomic data set (cd23_gf-5 of Kromer & Sim 2009) with only $\sim 400,000$ lines. This has been shown to give reliable results in the optical bands which, for our purposes, are the most important since they are the most different between our toy Model 3c and Model 3 of Fink et al. (2010). In the NIR bands, in contrast, Model 3c and Model 3 give rather similar results (see Figure 12).

The good agreement between our toy Model 3c and observational data does not only hold for band-limited light curves but also for individual spectral features as can be seen from Figure 11 which shows a spectrum of Model 3c at 3 days before B -band maximum. Compared to SN 2004eo, our toy model succeeds in reproducing the characteristic spectral features of intermediate-mass elements in SNe Ia. This is highlighted by our colour coding. Moreover, it shows an overall flux distribution which is in almost perfect agreement with the observed spectrum of SN 2004eo and we see no strong flux redistribution by titanium (compare with Model 3 in Figure 4).

This confirms our conclusion from Section 4.4 that the peculiarities of our model spectra with respect to the observations and their strong viewing-angle dependence are mainly due to the shell material and its compositional asymmetries. It also shows that the off-centre ignition of the secondary detonation in the C/O core causes only a minor viewing-angle dependence which is on the order of the observed variation between SNe Ia.

5.2. Prospects

In light of the discussion above, we are motivated to speculate on how the influence of the helium shell might be reduced. In the sub-Chandrasekhar-mass double detonation scenario, the helium shell cannot be removed entirely since it is required to trigger the detonation. Also the helium shell mass adopted in the Fink et al. (2010) models is already the minimum that might be expected to detonate (Bildsten et al. 2007). In Section 4, however, we have argued that the differences between our

model spectra and observations are not a consequence of the helium itself but of its particular burning products, namely titanium and chromium produced in the outer layers. The yields of these elements are affected by details of the nucleosynthesis in the shell.

The degree of burning in the shell material (and thus its final composition) can be affected by the initial abundance of heavy nuclei (e.g. ^{12}C) which in turn depend strongly on triple- α reactions during previous hydrostatic burning and dredge-up phases from the core (Shen & Bildsten 2009). Since the time-scale for α -captures behind the detonation shock front is significantly shorter than that of triple- α reactions, such seed-nuclei can limit the α -chain before reaching nuclear statistical equilibrium. If, for example, in a shell consisting of a mixture of ^4He and ^{12}C the number ratio of free α -particles to ^{12}C -nuclei on average is less than 6 (corresponding to a mass ratio of 2), the α -chain will end at ^{36}Ar . Thus, it is possible that more intermediate-mass elements and less titanium and chromium may be produced. Therefore it is interesting to consider how the burning of the helium might be different from that found by Fink et al. (2010) for different initial compositions of the shell. A full study of this goes beyond the scope of this work and will be published in a follow-up study. Here, we illustrate the possibility of obtaining better agreement with data for just one example.

In the Fink et al. (2010) models it was initially assumed that the shell consisted of pure helium. To demonstrate the sensitivity to the initial composition of the shell, we set up another toy model. For this “modified” model (hereafter 3m), we homogeneously polluted the shell of Model 3 with 34% (by mass) of ^{12}C and repeated the hydrodynamics and nucleosynthesis calculation (in the same way as described by Fink et al. 2010)¹. We found that a core detonation was still triggered but the different shell burning led to a substantial reduction of the mass of ^{44}Ti , ^{48}Cr and ^{52}Fe in the shell (nucleosynthetic yields for core and shell of the model are given in Table 1). Since the detonation tables of Fink et al. (2010) are only valid for pure helium, Model 3m is not fully self-consistent. Nevertheless, it is a useful toy model to explore the basic effect of a modified shell composition.

Figure 12 compares the angle-averaged band-limited light curves of this modified model (3m), to those of Model 3 of Fink et al. (2010) and our core-only toy model (3c). As can be seen, the modified Model 3m produces light curves very similar to those of Model 3c despite having about the same shell mass as Model 3. The most obvious difference between our modified and core-only models occurs in the U band: the titanium in the outer layer of Model 3m causes some line blocking, leading generally to a dimmer U -band magnitude than for Model 3c which has no outer layer. Compared to Model 3, with its large titanium mass in the shell, however, this effect is much weaker. The B band, which is strongly affected in Model 3, shows no significant titanium absorption for Model 3m. Another slight difference between Model 3m

¹ We note, that the base temperature of the shell in Model 3m was decreased to 4×10^8 K (compared to 6.7×10^8 K in Model 3) to suppress further triple- α burning in the shell. As a consequence the density and also the shell mass changes slightly compared to the original Model 3 (cf. Table 1).

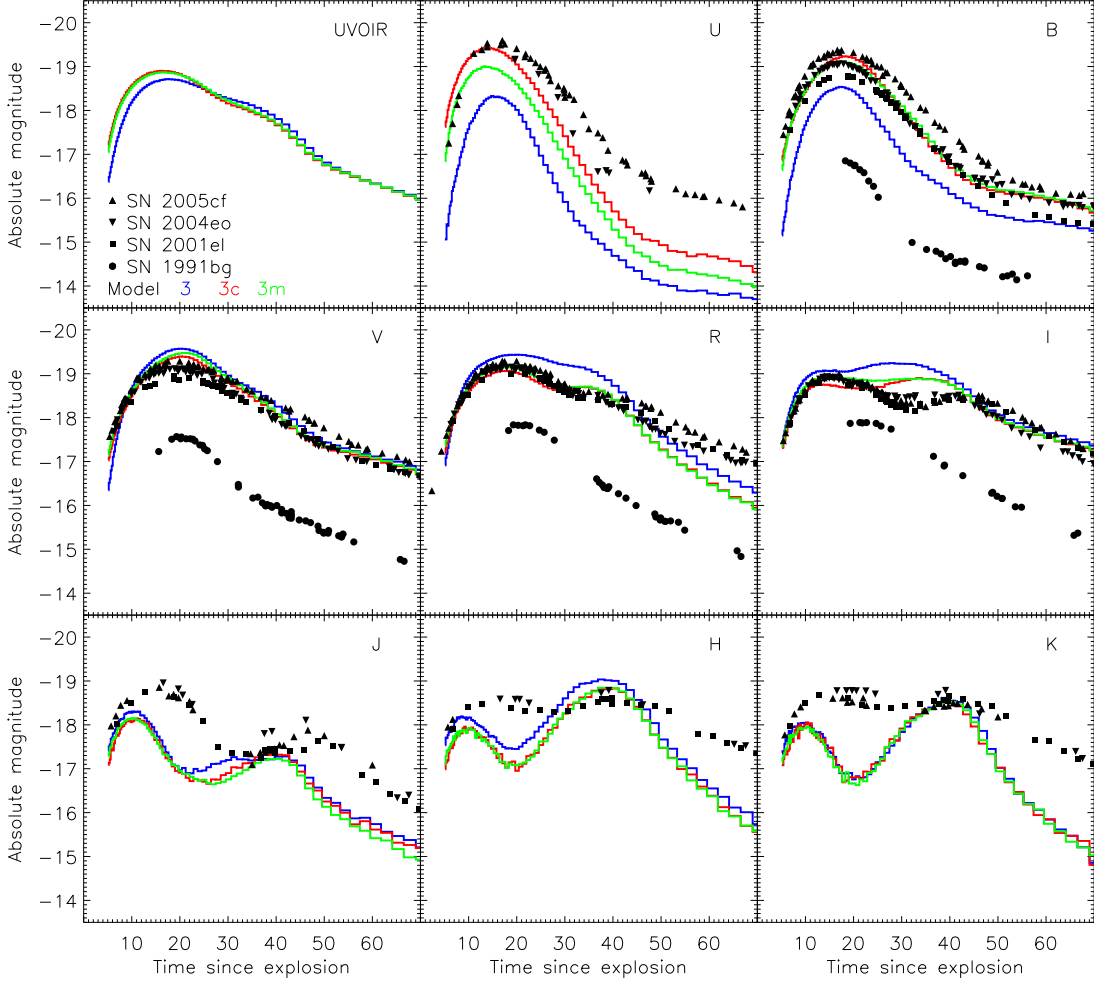


Figure 12. Angle-averaged *UVOIR* bolometric and *U, B, V, R, I, J, H, K* band-limited light curves for Model 3, 3c and 3m of our model sequence as indicated by the colour coding (compare Table 1 for details on the models). For comparison angle-averaged light curves (black dashed) and photometrical data of our fiducial SNe 2005cf, 2004eo, 2001el and 1991bg (different symbols) are shown.

and 3c occurs after the first peak in the *I* band. Comparing the light curves of Model 3m to SN 2004eo, we find qualitatively similar agreement as for Model 3c.

This generally also holds for the angle-averaged spectrum at 3 days before *B*-band maximum, shown in Figure 13. Compared to Model 3c, where the agreement was almost perfect, there are some minor shortcomings. But the model is dramatically improved compared to Model 3 of Fink et al. (2010). The small differences between Model 3c and 3m are again mostly due to the titanium in the outer layers which leads to pronounced absorption troughs bluewards of the Ca II H and K lines and redwards of 4,000 Å. This suggests that Model 3m still over-produced titanium in the shell. Interestingly, the enhanced calcium abundance in the outer layers (cf. Table 1) leads to a stronger Ca II NIR triplet, bringing the model in better agreement with the spectrum of SN 2004eo at the corresponding epoch. Therefore some *calcium* in the outer shell is an *improvement* over Model 3c. This suggests that a slight further reduction in the degree of burning so that titanium is further suppressed in favour of calcium (just one step down the α -chain) could lead to very good agreement.

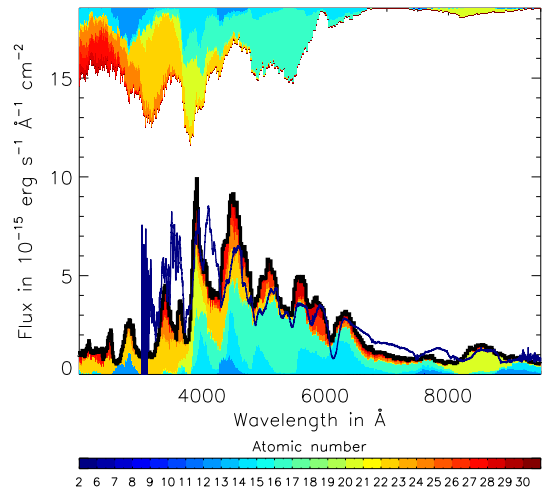


Figure 13. Angle-averaged (thick black line) spectra at three days before *B*-band maximum for Model 3m. For comparison the blue line shows the de-redshifted and de-reddened spectrum of SN 2004eo (Pastorello et al. 2007a) at the corresponding epoch. Note, that the flux is here in physical units and not scaled like in Figure 4. For a description of the colour coding see Figure 4.

In summary, polluting the initial helium shell of Model 3m with ^{12}C significantly improved the agreement between our synthetic spectra and light curves and those observed for SNe Ia making this model a promising progenitor candidate for SNe Ia. We stress again that this improvement results only from the change in the composition of the burning products of the helium shell which contains much less titanium and chromium for this model (the total shell mass stays about the same). Given that the initial composition of the helium shell depends on several processes including details of the accretion physics and hydrostatic burning phases that might precede the detonation or possible dredge-up of material from the C/O core, this leaves some scope to find sub-Chandrasekhar-mass double detonation models which give reasonable agreement with observed SNe Ia. This, however, must be investigated by future follow-up studies that more fully explore the influence of the initial composition of the helium shell on the burning products and link the initial composition of the helium shell directly to the evolution of progenitor models. Moreover, we note that different ignition geometries might also lead to better agreement with observational data. In particular, more symmetric ignition geometries, e.g. ignition in an equatorial ring or simultaneous ignition in multiple points (as studied by Fink et al. 2007 for the case of more massive helium shells), are likely to alleviate the strong viewing-angle dependence found for the point-like ignition of the Fink et al. (2010) models.

Our results also highlight the strong sensitivity of the radiative transfer to particular elements/ions (in our case titanium and chromium which represent only a tiny fraction of the ejecta mass yet dominate our conclusions). This emphasizes the need for a better description of nuclear reaction rates and continued study of the radiative transfer processes (and atomic data) in order to quantify more fully the systematic uncertainties which arise due to the complexity of spectrum formation in supernovae. In particular, we note that almost all the flux redistribution done by titanium and chromium in our models is due to their singly ionized states. Since the current ionization treatment of ARTIS neglects non-thermal processes (see Kromer & Sim 2009 for more details), we cannot exclude that the actual ionization state in the helium shell ejecta would be higher due to non-thermal ionization from the radioactive isotopes produced during the helium burning. This could also significantly improve the agreement between our models and observational data, as a numerical experiment with an artificially enforced higher ionization state for titanium and chromium has shown.

6. CONCLUSION

In this paper we presented synthetic observables for the sub-Chandrasekhar-mass double detonation models of Fink et al. (2010). We found that these models predict light curves which rise and fade on time-scales typical of SNe Ia. Moreover, they produce a large range of brightnesses which covers the whole range of observed SNe Ia. However, they do not account for all the properties of observed SNe Ia since they have peculiar spectra and light curves. In particular, their $B - V$ colours are generally too red compared to observed SNe Ia. This is in contrast to the results of earlier work on models with more massive helium shells (Höflich & Khokhlov 1996;

Höflich et al. 1996; Nugent et al. 1997). In addition, our model light curves and spectra show an unreasonably strong viewing-angle dependence due to the point-like ignition of the Fink et al. (2010) models and the resulting ejecta asymmetries.

Detonation of a pure helium shell leads to a layer containing iron-group elements like titanium and chromium around the core ejecta. These elements have a vast number of optically thick lines in the UV and blue part of the spectrum making them very effective in blocking the flux in these wavelength regions and redistributing it to the red. We used a toy model to show that this layer of titanium and chromium causes the peculiar red colours of our light curves and also the peculiar spectral features. Moreover, we found that this toy model reproduces the observed properties of SNe Ia remarkably well. The toy model also showed that the strong viewing-angle dependence of our models results from the compositional asymmetry in the helium shell ejecta and not from the off-centre ignition of the C/O core. We stress, that the additional energy release in the shell, due to the production of radioactive nuclides during the helium burning, is relatively inconsequential for our models – even at γ -ray energies the signatures of the surface ^{48}Cr and ^{52}Fe are not apparent. Instead, in the optical/UV the shell has a strong signature but this is primarily due to the additional opacity in the outer layers which affects the transport of energy from the core to the surface. We conclude that, if the double detonation sub-Chandrasekhar-mass model valid for normal SNe Ia, the properties of the post-burning helium shell material need to be different from those in the Fink et al. (2010) models.

Since Fink et al. (2010) considered the limit of the least massive helium shells which might ignite a detonation in the helium shell, their models represent the most optimistic case for reducing the influence of the shell material by simply reducing the shell mass. However, we argue that the mass of the helium shell ejecta is not the main problem but rather the peculiar composition including comparably large masses of titanium and chromium. We illustrated this using a second toy model, where the initial composition of the helium shell was polluted with 34% (by mass) of ^{12}C . By providing additional seed-nuclei for α -captures, this leads to burning products with lower atomic number (i.e. intermediate-mass elements rather than mainly iron-group elements). Spectra and light curves of this model which has about the same shell mass as Model 3 of Fink et al. (2010) show comparably good agreement to observed SNe Ia as the shell-less toy model.

Taking into account all these results, we argue that these systems might yet be promising candidates for SN Ia progenitors. Much more work will be needed to properly investigate this possibility. Besides a more detailed description of the excitation/ionization state in the radiative transfer modelling which includes non-thermal effects, we need a better understanding of the initial composition of the helium shell and the incomplete burning processes which take place in this material to reach reliable predictions of the burning products of the helium shell. Although only a tiny fraction of the mass, the post-burning composition of the shell material is critical to assessing the viability of the sub-Chandrasekhar-mass double detonation scenario.

ACKNOWLEDGMENTS

We thank R. Pakmor and S. Taubenberger for many helpful comments and our referee, David Branch, for a supportive report. The simulations presented here were carried out at the Computer Center of the Max Planck Society in Garching, Germany. This work was supported by the Deutsche Forschungsgemeinschaft via the Transregional Collaborative Research Center TRR 33 “The Dark Universe”, the Excellence Cluster EXC153 “Origin and Structure of the Universe” and the Emmy Noether Program (RO 3676/1-1).

REFERENCES

- Ambwani, K., & Sutherland, P. 1988, *ApJ*, 325, 820
 Arnett, W. D., Truran, J. W., & Woosley, S. E. 1971, *ApJ*, 165, 87
 Bildsten, L., Shen, K. J., Weinberg, N. N., & Nelemans, G. 2007, *ApJ*, 662, L95
 Burrows, T. W. 2006, *Nuclear Data Sheets*, 107, 1747
 Colgate, S. A., & McKee, C. 1969, *ApJ*, 157, 623
 Di Stefano, R. 2010, *ArXiv e-prints*
 Dolag, K., & Stasyszyn, F. 2009, *MNRAS*, 398, 1678
 Filippenko, A. V., et al. 1992, *AJ*, 104, 1543
 Fink, M., Hillebrandt, W., & Röpke, F. K. 2007, *A&A*, 476, 1133
 Fink, M., Röpke, F. K., Hillebrandt, W., Seitenzahl, I. R., Sim, S. A., & Kromer, M. 2010, *A&A*, 514, A53+
 Garnavich, P. M., et al. 2004, *ApJ*, 613, 1120
 Gilfanov, M., & Bogdán, Á. 2010, *Nature*, 463, 924
 Gómez-Gomar, J., Isern, J., & Jean, P. 1998, *MNRAS*, 295, 1
 Hayden, B. T., et al. 2010, *ApJ*, 712, 350
 Hicken, M., et al. 2009, *ApJ*, 700, 331
 Hillebrandt, W., & Niemeyer, J. C. 2000, *ARA&A*, 38, 191
 Hillebrandt, W., Sim, S. A., & Röpke, F. K. 2007, *A&A*, 465, L17
 Höflich, P., & Khokhlov, A. 1996, *ApJ*, 457, 500
 Höflich, P., Khokhlov, A., Wheeler, J. C., Phillips, M. M., Suntzeff, N. B., & Hamuy, M. 1996, *ApJ*, 472, L81+
 Howell, D. A., et al. 2006, *Nature*, 443, 308
 Kasen, D. 2006, *ApJ*, 649, 939
 Kasen, D., Röpke, F. K., & Woosley, S. E. 2009, *Nature*, 460, 869
 Khokhlov, A. M. 1991, *A&A*, 245, 114
 Krisciunas, K., et al. 2003, *AJ*, 125, 166
 Kromer, M., & Sim, S. A. 2009, *MNRAS*, 398, 1809
 Leibundgut, B., et al. 1993, *AJ*, 105, 301
 Lira, P. 1995, Master’s thesis, Univ. Chile
 Livne, E., & Arnett, D. 1995, *ApJ*, 452, 62
 Lucy, L. B. 2005, *A&A*, 429, 19
 Mannucci, F., Della Valle, M., Panagia, N., Cappellaro, E., Cresci, G., Maiolino, R., Petrosian, A., & Turatto, M. 2005, *A&A*, 433, 807
 Meng, X., & Yang, W. 2010, *ApJ*, 710, 1310
 Milne, P. A., et al. 2004, *ApJ*, 613, 1101
 Nomoto, K., Thielemann, F.-K., & Yokoi, K. 1984, *ApJ*, 286, 644
 Nugent, P., Baron, E., Branch, D., Fisher, A., & Hauschildt, P. H. 1997, *ApJ*, 485, 812
 Pastorello, A., et al. 2007a, *MNRAS*, 377, 1531
 —. 2007b, *MNRAS*, 376, 1301
 Phillips, M. M. 1993, *ApJ*, 413, L105
 Ruiter, A. J., Belczynski, K., & Fryer, C. 2009, *ApJ*, 699, 2026
 Scannapieco, E., & Bildsten, L. 2005, *ApJ*, 629, L85
 Shen, K. J., & Bildsten, L. 2009, *ApJ*, 699, 1365
 Sim, S. A. 2007, *MNRAS*, 375, 154
 Sim, S. A., & Mazzali, P. A. 2008, *MNRAS*, 385, 1681
 Sim, S. A., Röpke, F. K., Hillebrandt, W., Kromer, M., Pakmor, R., Fink, M., Ruiter, A. J., & Seitenzahl, I. R. 2010, *ApJ*, 714, L52
 Sim, S. A., Sauer, D. N., Röpke, F. K., & Hillebrandt, W. 2007, *MNRAS*, 378, 2
 Taubenberger, S., et al. 2008, *MNRAS*, 385, 75
 Thielemann, F.-K., Nomoto, K., & Yokoi, K. 1986, *A&A*, 158, 17
 Truran, J., Arnett, D., & Cameron, A. 1967, *Canad. J. Physics*, 45, 2315
 Woosley, S. E., & Weaver, T. A. 1994, *ApJ*, 423, 371